RSC Advances

PAPER

View Article Online
View Journal | View Issue

Cite this: *RSC Adv.*, 2018, **8**, 4321

A theranostic nanocomposite system based on radial mesoporous silica hybridized with Fe_3O_4 nanoparticles for targeted magnetic field responsive chemotherapy of breast cancer†

Qin Gao,[ab] Wensheng Xie,[ab] Yu Wang,[ab] Dan Wang,[ab] Zhenhu Guo,[c] Fei Gao,[d] Lingyun Zhao*[ab] and Qiang Cai*[ab]

Achieving accumulation of a target drug in tumor tissue, optimal release behavior and concurrent diagnostic imaging with therapy (theranostic) requires an ideal chemotherapy protocol that involves the responsive control of drug delivery. In the current study, we report the construction of a novel theranostic drug delivery system based on radial mesoporous silica, which is hybridized with multiscale magnetic nanoparticles for MRI-guided and alternative magnetic field (AMF) responsive chemotherapy for breast cancer. Superparamagnetic iron oxide nanoparticles (IONPs) with multiscale sizes were prepared *via* a hydrothermal method (for larger IONPs, lIO NPs) and a thermal decomposition method (for ultra-small IONPs, uIO NPs). lIO NPs act as the heat mediator that is responsive to the AMF, while uIO NPs act as the T_2 contrast agent for MRI. Mesoporous silica nanoparticles with radially oriented mesochannels were further *in situ* grown onto the surfaces of the lIO NPs, and both the uIO NPs and doxorubicin, an anti-cancer drug, can be readily incorporated within the mesochannels. To endow the as-prepared doxorubicin-loaded nano-hybrids with a good targeting ability, the surfaces of the particles were modified with folic acid (FA). This prepared drug delivery system based on magnetic/silica nanocomposites showed high drug loading efficiency and AMF stimuli responsive release properties. Meanwhile, *in vitro* MRI measurements revealed an excellent MRI contrast effect with a high relaxation value of 308 mM^{-1} s^{-1}. Furthermore, both *in vitro* cytotoxicity analysis and *in vivo* anti-tumor effect evaluation demonstrated that the drug delivery system possesses great potential as an MRI-guided stimuli-responsive theranostic platform for effective active targeting chemotherapy of cancer.

Received 15th November 2017
Accepted 2nd January 2018

DOI: 10.1039/c7ra12446e

rsc.li/rsc-advances

Introduction

Since the first anti-cancer drug was approved by the Food and Drug Administration (FDA) to treat hematological cancer, chemotherapy has been recognized as one of the key components of treatment for all stages of cancers, including early stage disease and patients with complete resection.[1–3] However, despite an expanding panel of chemotherapeutic agents such as paclitaxel, docetaxel, vincristine, pemetrexed, topotecan and irinotecan that show high effectiveness, the severe side effects of chemotherapy continues to be one of the significant challenges during the treatment, due to the high dosage and indiscriminate delivery of chemotherapeutic agents.[4,5] Drug delivery systems based on nanotechnology are encouraging administration platforms for the efficient delivery of drugs to lesions and targeting sites, to avoid ineffective treatment from under-dosing or toxicity due to overdosing.[6–9] Furthermore, when these delivery systems exhibit controlled release behavior, the drug levels can be administered continuously within a desired therapeutic range for a long period of time.

Over the last decade, various drug delivery systems, such as micelles, liposomes, multifunctional dendritic polymers, nanospheres, nanocapsules, hydrogels and liquid crystals, have been successfully developed for efficient passive- or active-targeting delivery strategies.[10–13] Although each system possesses its own advantages, several significant limitations often affect their further application. For instance, micelles and liposomes may suffer from poor chemical stability and disintegration due to the high-density lipoproteins used.[14,15]

[a]State Key Laboratory of New Ceramics and Fine Processing, School of Materials Science & Engineering, Tsinghua University, Beijing 100084, China. E-mail: lyzhao@mail.tsinghua.edu.cn; caiqiang@mail.tsinghua.edu.cn

[b]Advanced Materials of Ministry of Education of China, School of Materials Science and Engineering, Tsinghua University, Beijing, 100084, China

[c]School of Earth Sciences and Resources, China University of Geosciences, Beijing, 10083, China

[d]College of Chemistry and Materials Science, Northwest University, Xi'an, Shanxi, 710069, China

† Electronic supplementary information (ESI) available. See DOI: 10.1039/c7ra12446e

Meanwhile, toxicity problems are the main obstacles hindering the applications of synthesized polymers, nanospheres and hydrogels, due to the problems of *in vivo* degradation, while dendrimers are limited by their quick elimination by the liver and kidneys and low blood stability.[16] Currently, mesoporous silica and oxidized porous silicon have attracted great attention in drug delivery research, as both materials exhibit high surface area, thermal stability, tunable pore size, chemical inertness, excellent biocompatibility, and biodegradability.[17–19] The large surface area and porous interior make these materials excellent reservoirs for delivering hydrophobic drugs, and their tunable pore size can be tailored to selectively store different nanoparticles and molecules of interest. In addition, the simple and adjustable synthesis process makes it easy to obtain optimized sizes and shapes for maximum cellular uptake.[20,21] Furthermore, the ease of modifying the surface of mesoporous silica makes it possible to design active-targeting and stimuli-responsive drug delivery systems.

To achieve precise chemotherapy of cancer, the drug delivery system used must be site-specific and time-release controlled.[22] Compared to passive-targeting offered by the enhanced permeability and retention effect (EPR effect), active-targeting strategies such as attaching an antibody, carrier protein or a ligand to the drug delivery system will allow it to accumulate at a target location, thus obtaining high efficacy with low dosage and low side effects and toxicity.[23,24] Meanwhile, the controlled release of drugs from delivery systems can be triggered by various internal or external stimuli such as heat, light, an electric field, an alternative magnetic field (AMF), pH, redox, enzyme activity, mechanical force and so on.[25,26] Among them, AMF-sensitive systems, which can be induced by integration with supermagnetic iron oxide nanoparticles, show great potential for triggering drug release due to their safety, high penetration depth and lack of radiotoxicity.[27,28] Furthermore, supermagnetic iron oxide nanoparticles loaded in a drug delivery system can be used as the T_2-weighted MRI contrast agent to evaluate the targeting ability of the delivery system and to evaluate the therapeutic effect in real time.[29,30] Therefore, developing an effective delivery system with high drug loading efficiency, active-targeting and stimuli-responsive behavior, along with a concurrent diagnostic method with therapy (theranostic), is essential for efficient cancer chemotherapy.

Herein, in the current study, we report a novel theranostic drug delivery system based on radial mesoporous silica, which is hybridized with multiscale MNPs, for MRI-guided and AMF-responsive chemotherapy for breast cancer. Superparamagnetic iron oxide nanoparticles (IONPs) with multiscale sizes were prepared *via* a hydrothermal method (for larger IONPs, lIO NPs) and a thermal decomposition method (for ultra-small IONPs, uIO NPs), lIO NPs act as the mediator that is responsive to the AMF, and uIO NPs act as the T_2 contrast agent for MRI. Mesoporous silica spheres with radially oriented mesochannels were further *in situ* grown onto the surfaces of the lIO NPs (IOMSN NPs), and both the uIO NPs and doxorubicin, an anti-cancer drug, can be readily incorporated within the mesochannels (IOMSN@uIO(DOX) NPs). To endow the as-prepared doxorubicin-loaded nano-hybrids with good targeting ability, the surfaces of the particles were modified with folic acid (FA) to obtain the final IOMSN@uIO(DOX)-FA NPs. The results show that the as-prepared silica/magnetic nano-hybrids possess uniform size and excellent drug loading, delivery efficiency and MRI contrast effect. Moreover, a series of detailed *in vitro* biocompatibility and H&E staining analysis of these nano-hybrids revealed excellent biocompatibility, even at a high concentration of 200 μg mL^{-1}. Furthermore, both *in vitro* cytotoxicity analysis and *in vivo* cytotoxicity anti-tumor effect evaluation demonstrated that IOMSN@uIO(DOX)-FA NPs are an excellent drug delivery system that possesses great potential as an MRI-guided stimuli-responsive drug delivery system theranostic platform for effective active targeting chemotherapy of cancer.

Results and discussion

Synthesis and characterization of IOMSN@uIO-FA NPs

The synthetic process for the uniform radial IOMSN@uIO(DOX)-FA NPs through a simple soft-template method is illustrated in Scheme 1. Firstly, lIO NPs were prepared *via* a one-pot hydrothermal method.

Both the scanning electron microscopy (SEM) image (Fig. 1a1) and the transmission electron microscopy (TEM) image (Fig. 1a2) show that the as-prepared lIO NPs have an irregular spherical shape with a uniform diameter of ~42 nm. Then, IO-NH_2 MNPs were used as the soft-template for the synthesis of IOMSN NPs. As shown in Fig. 1b1, the NPs have a mean diameter of about 750 nm and consist of a radially oriented irregular mesostructure, which was further confirmed by the TEM image (Fig. 1b2). The continuous radial mesostructure throughout indicates that this kind of mesoporous IOMSN NPs would favor the loading or adsorption and release of guest nanoparticles or molecules, such as anti-cancer therapeutic agents. To verify the components of the IOMSN NPs, X-ray powder diffraction (XRD) was conducted, and the

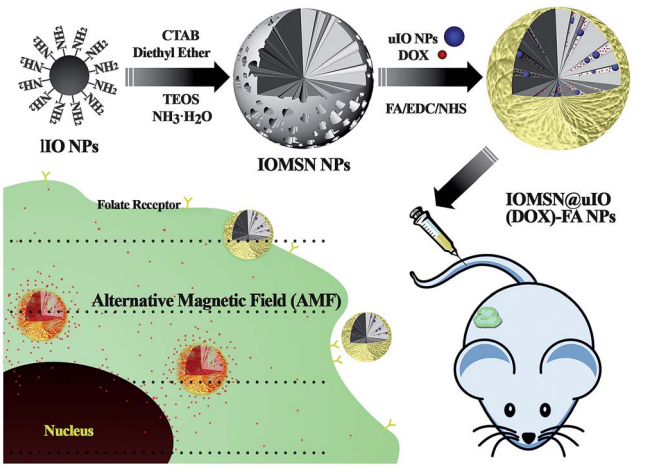

Scheme 1 Schematic illustration depicting the preparation of IOMSN@uIO(DOX)-FA NPs and their application as an MRI-guided stimuli-responsive theranostic platform for effective active targeting chemotherapy of cancer.

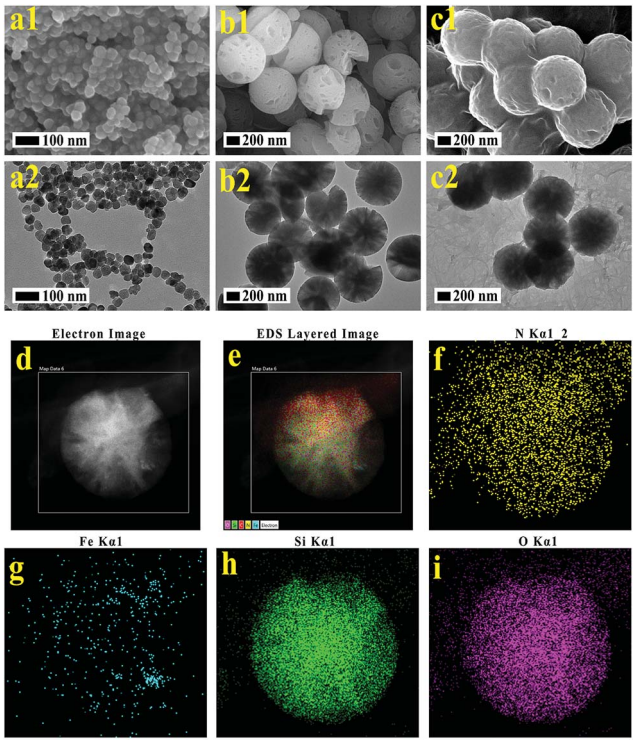

Fig. 1 Characterization of the as-synthesized lIO NPs, IOMSN NPs, IOMSN-FA NPs and IOMSN@uIO-FA NPs. SEM images and TEM images of lIO NPs (a1, a2), IOMSN NPs (b1, b2), and IOMSN-FA NPs (c1, c2). (d–i) HRTEM image of IOMSN@uIO-FA NPs and relevant EDS elemental maps for the elements N (f), Fe (g), Si (h) and O (i).

spectrum (Fig. 2a) shows that the characteristic peaks of (220), (311), (400), (511) and (440) are compatible with the iron oxide crystal structure, while the peak at $2\theta = 23^{\circ}$ reveals the existence of an amorphous silica structure. Finally, IOMSN-FA NPs and IOMSN@uIO-FA NPs were synthesized *via* modification of the surfaces with FA and loading uIO NPs in the radial mesostructure of IOMSN NPs using a crosslinker. After APTES was conjugated on the surface of IOMSN NPs to obtain IOMSN-NH_2 NPs, EDC could easily react with the carboxylic acid groups of FA to form an active *O*-acylisourea intermediate, which was easily displaced by nucleophilic attack from the primary amino groups of the pre-prepared IOMSN-NH_2 NPs in the reaction mixture. Fig. 1c1 clearly shows that the radial mesostructure of IOMSN-FA NPs was blocked by FA, thus resulting in a rougher surface (Fig. 1c2) compared to the IOMSN NPs. After loading with uIO NPs in the radial mesostructures, the final IOMSN@uIO-FA NPs were obtained. The HRTEM images clearly demonstrate the morphology of the uIO NPs (Fig. S1a†) and the radial-type amorphous silica structure of the IOMSN@uIO-FA NPs (Fig. S1b†), which was further confirmed by the corresponding element mapping (Fig. 1d–i). Furthermore, after being suspended in DI water homogenously and then placed beside a magnet for 1 min, all the IOMSN@uIO-FA NPs gathered close to the magnet (Fig. S2†), confirming the successful integration of IOMSN NPs and uIO NPs.

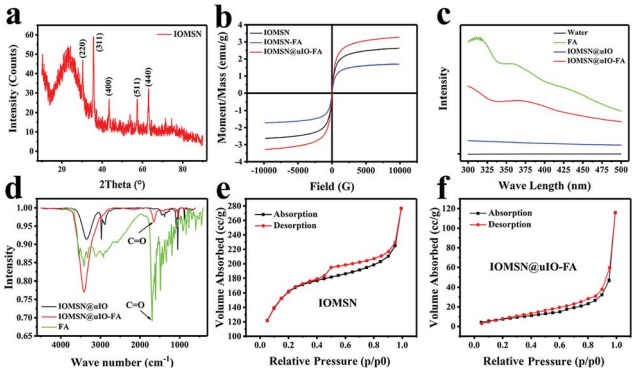

Fig. 2 (a) XRD spectrum of the IOMSN NPs. (b) Magnetization hysteresis loops of the IOMSN NPs, IOMSN-FA NPs and IOMSN@uIO-FA NPs. (c) UV-vis absorption spectra of DI water, FA, IOMSN@uIO NPs and IOMSN@uIO-FA NPs. (d) FTIR spectra of the IOMSN@uIO NPs, IOMSN@uIO-FA NPs and FA. Nitrogen sorption isotherms of the IOMSN NPs (e) and IOMSN@uIO-FA NPs (f).

Fig. 2b shows the hysteresis loops of the IOMSN NPs, IOMSN-FA NPs and IOMSN@uIO NPs measured at room temperature. All the NPs showed supermagnetic behavior with saturation magnetization (M_s) values of 2.64, 1.68 and 3.28 emu g^{-1}, respectively. The supermagnetic property of the IOMSN NPs indicates that the lIO NPs had successfully acted as the soft-template to prepare the NPs and had then been encapsulated in it. Meanwhile, the modification with FA weakened the magnetic property of the IOMSN-FA NPs, while the higher M_s of the IOMSN@uIO-FA NPs compared to the IOMSN NPs and IOMSN-FA NPs directly demonstrates the successful loading of uIO NPs in the radial mesostructure of the IOMSN@uIO-FA NPs. To further evaluate the FA on the IOMSN@uIO-FA NPs, UV-vis absorbance spectroscopy and FTIR spectroscopy were performed for FA, IOMSN@uIO NPs and IOMSN@uIO-FA NPs. The IOMSN@uIO-FA NPs showed a characteristic absorbance peak at ~360 nm, which corresponds to the absorption spectra of FA. In addition, the FTIR results indicate successful FA modification due to the existence of the C=O bond at 1679 cm^{-1}. The nitrogen sorption isotherm of the IOMSN NPs (Fig. 2e) shows a type IV curve according to the IUPAC nomenclature, with a hysteresis loop in the 0.4–1.0 p/p_0 range, demonstrating the narrow pore size distribution of the IOMSN NPs. In addition, the IOMSN@uIO-FA NPs show a type II curve with a larger p/p_0 range of 0.3–1.0 and a low surface area of 68.44 m^2 g^{-1} compared to 477.68 m^2 g^{-1} for the IOMSN@uIO-FA NPs, revealing the loading of the uIO NPs and encapsulation of FA.

In vitro cytotoxicity and cell uptake of IOMSN@uIO-FA NPs

As is well known, the biocompatibility and cytotoxicity of a drug delivery system are of great significance for its application in the field of nanomedicine.[31] Therefore, the cytotoxicity of the IOMSN@uIO-FA NPs against the L929 cell line was investigated using the CCK-8 assay. It was found that the L929 cells exhibited a higher cell viability of more than 90.4%, even when incubated with a high IOMSN@uIO-FA NP concentration of 200 μg mL^{-1} for 24 h and 48 h (Fig. 3). Although the cell viability at a concentration of 500 μg mL^{-1} decreased somewhat after 48 h

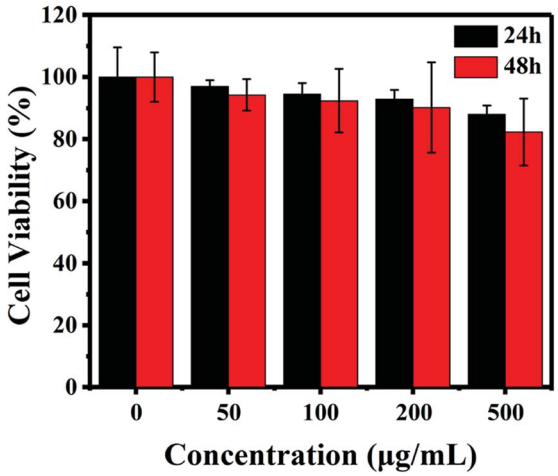

Fig. 3 The viabilities of L929 cells after incubation with different concentrations (0, 50, 100, 200, 500 μg mL^{-1}) of IOMSN@uIO-FA NPs for 24 h and 48 h. Data are presented as mean ± standard deviation ($n = 5$).

of incubation, the cell viability was still as high as 82.5%, indicating that the IOMSN@uIO-FA NPs could be used as a drug delivery system. The excellent cell uptake offered by the active targeting strategies of drug delivery systems is an effective way to enhance the delivery efficiency and chemotherapy effect.[32] The cell uptake of coumarin-6-loaded IOMSN@uIO NPs and IOMSN@uIO-FA NPs were investigated using a confocal laser scanning microscope. Fig. 4 shows the increasing amount of NPs internalized in MCF-7 cells with increasing incubation time. Obviously, the efficiency of cell uptake for the IOMSN@uIO-FA NPs was much higher than that for the IOMSN@uIO NPs, which indicates that FA could enhance the cell uptake efficiency of IOMSN@uIO NPs *via* the folate receptor, which was further confirmed by the 3-dimensional CLSM images (Fig. S3†). All the NPs were located in the matrix of MCF-7 cells crossing the cell membranes.

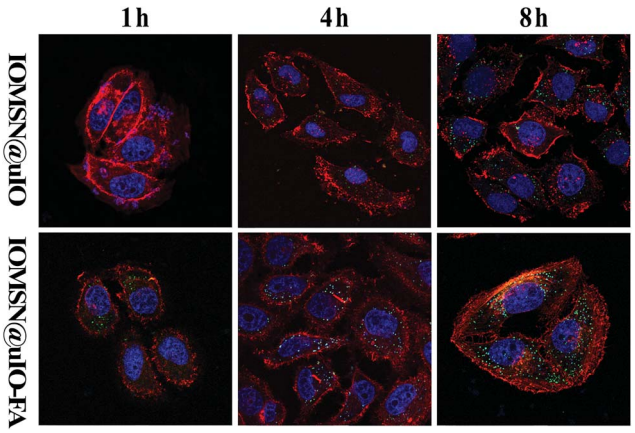

Fig. 4 Cellular uptake efficiency of the IOMSN@uIO NPs and IOMSN@uIO-FA NPs in MCF-7 cells (concentration is 50 μg mL^{-1}). The nuclei of cells were stained with DAPI (blue) and the cytoskeleton was stained with rhodamine phalloidin (red). Coumarin-6-loaded nanoparticles (green) were used to track the distribution.

In vitro release profiles of DOX

A high drug loading efficiency and smart release properties are essential characteristics to measure when evaluating a drug delivery system. Doxorubicin (DOX) was chosen as a model anticancer drug to test the IOMSN@uIO-FA NPs. The results show that the loading efficiency of DOX in the IOMSN@uIO-FA NPs was 86.21 ± 3.34%, and the DOX loading amount was 0.46 μg in 1 μg of the IOMSN@uIO(DOX)-FA NPs. The release profiles of DOX from the IOMSN@uIO(DOX)-FA NPs with or without exposure to an AMF (13.33 kA m^{-1}, 282 kHz) in PBS at 37 °C are shown in Fig. 5b. It was clearly found that the release of DOX was time-dependent and sustained-release behavior was observed.

Within 300 h, the accumulative release amount of DOX reached 83.11% without exposure to an AMF. In comparison, after being exposed to an AMF every day, the release speed of DOX was increased and a total of 91.04% of DOX was released from the IOMSN@uIO(DOX)-FA NPs, which was 1.1 times higher than that achieved without exposure. Superparamagnetic iron oxide nanoparticles can generate heat under an AMF due to the Néel relaxation and Brown relaxation.[33] The temperature response curve for the IOMSN@uIO(DOX)-FA NP suspension in DI water with a concentration of 100 μg mL^{-1} under an AMF (13.33 kA m^{-1}, 282 kHz) is shown in Fig. 5a. After exposure for 10 min, a temperature increase of 4.8 °C was obtained. Therefore, we speculated that the heat induced by iron oxide in the IOMSN@uIO-FA NPs under the AMF accelerated the release of DOX by accelerating the thermal motion of DOX molecules.

In vitro cytotoxicity of IOMSN@uIO(DOX)-FA NPs

The *in vitro* AMF stimuli-responsive property of DOX release inspired us to use an external AMF to control the release of DOX for enhanced chemotherapy efficacy. Herein, the cytotoxic effects of the IOMSN@uIO(DOX) NPs and IOMSN@uIO(DOX)-FA NPs, with or without AMF exposure against MCF-7 cells were tested. The results (Fig. 6) show that all the NPs exhibited time-dependent cell proliferation inhibition compared to a control group. The IOMSN@uIO(DOX)-FA NPs revealed higher

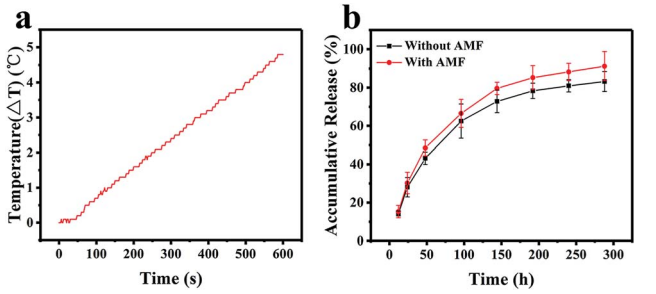

Fig. 5 (a) Hyperthermia study showing the time-dependent temperature profiles of the IOMSN@uIO-FA NPs at a concentration of 100 μg mL^{-1} and with exposure to 13.33 kA m^{-1} AMF at 282 kHz. (b) Accumulative release profile of DOX from the IOMSN@uIO(DOX)-FA NPs at 37 °C with and without exposure to an AMF for 10 min each day (13.33 kA m^{-1}, 282 kHz).

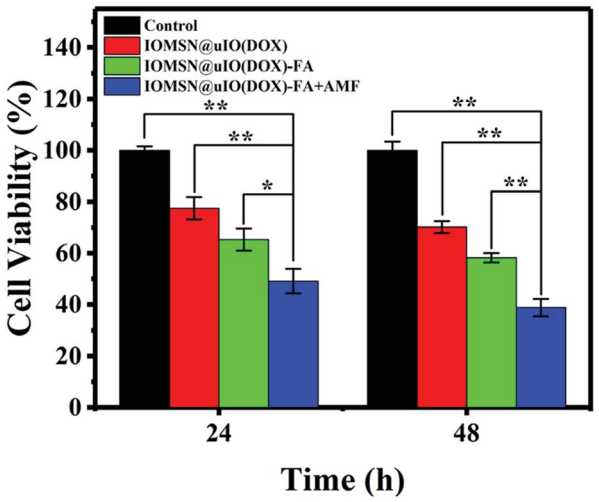

Fig. 6 The viabilities of MCF-7 cells incubated with IOMSN@uIO(DOX) NPs and IOMSN@uIO(DOX)-FA NPs at a concentration of 100 μg mL^{-1} for 24 h and 48 h. For the AMF-triggered chemotherapy group, the cells incubated with the IOMSN@uIO(DOX)-FA NPs were exposed to an AMF with a power of 13.33 kA m^{-1} (282 kHz) for 10 min. Data are presented as mean ± standard deviation ($n = 5$). *$p < 0.05$, **$p < 0.005$.

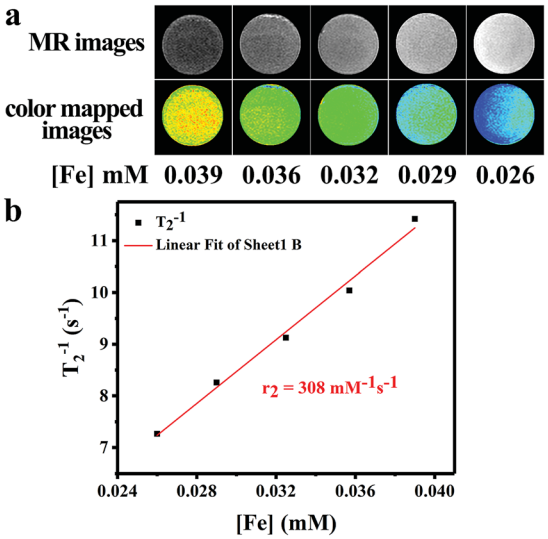

Fig. 7 (a) *In vitro* phantom MRI contrast images and color mapped images of the IOMSN@uIO-FA NPs at different concentrations of 0.026, 0.029, 0.032, 0.036 and 0.039 mM [Fe]. (b) Linear fitting of $1/T_2$ value in terms of different concentrations of Fe.

cytotoxicity to MCF-7 cancer cells than the IOMSN@uIO(DOX) NPs, as modification with FA could increase the amount of NPs taken up by cells *via* FA receptor-mediated endocytosis. Thus, more DOX would be released inside the cells and cause more cell death. Importantly, for the IOMSN@uIO(DOX)-FA NPs group, which were exposed to an AMF (13.33 kA m^{-1}, 282 kHz) for 10 min, a more efficient anti-cancer effect was obtained with a low cell viability of 38.86% after 48 h of incubation compared to 58.26% without exposure. Therefore, the IOMSN@uIO(DOX)-FA NPs with active targeting and stimuli-responsive properties show great potential for targeting cancer tissues and enhancing chemotherapy *in vivo*.

In vitro MRI measurements

To evaluate the T_2-weighted MR imaging contrast effect of the IOMSN@uIO-FA NPs, a 3.0 T whole-body MR scanner was used to obtain T_2-weighted MR images of the IOMSN@uIO-FA NPs suspended in DI water with different Fe concentrations of 0.026, 0.029, 0.032, 0.036 and 0.039 mM (Fig. 7). The Fe concentration of the IOMSN@uIO-FA NPs was determined using inductively coupled plasma optical emission spectrometry (ICP-OES). As shown in Fig. 7a, the IOMSN@uIO-FA NPs induced a dark signal enhancement in a concentration-dependent manner. With increasing Fe concentration, a stronger signal (dark signal) was obtained, which was further confirmed by the transverse relaxivity values (r_2) (Fig. 7b). The r_2 value of the IOMS@uIO-FA NPs was 308 mM^{-1} s^{-1} in terms of Fe, indicating that the IOMS@uIO-FA NPs show great potential as a contrast agent for T_2-weighted MR imaging of tumors.

In vivo anti-cancer efficacy

The excellent *in vitro* anti-cancer effect of the IOMS@uIO(DOX)-FA NPs against MCF-7 cells and prominent MR imaging behavior inspired us to further test the MRI-guided chemotherapy *in vivo*. Therefore, MCF-7 tumor-bearing mice were divided into five groups randomly ($n = 5$): control group, DOX group, IOMSN@uIO(DOX) group, IOMSN@uIO(DOX)-FA group and IOMSN@uIO(DOX)-FA + AMF group. Here, the DOX dosage of the DOX group was equivalent with that of the NP groups. All agents were intravenously (i.v.) injected through the tail vein of the mice and the therapeutic efficacy was evaluated by measuring the relevant tumor volume (Fig. 8a) and body weight

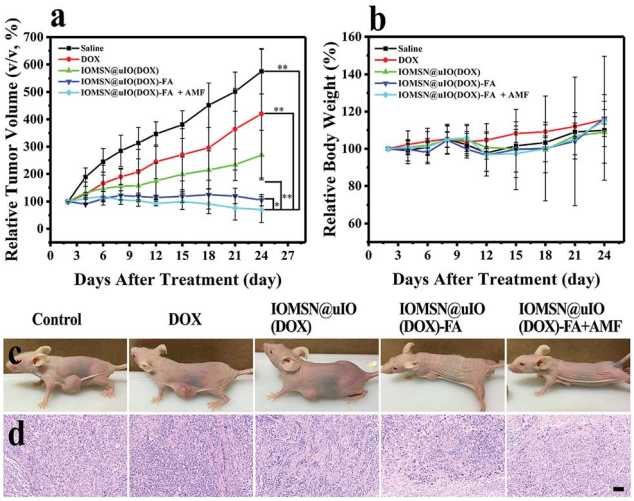

Fig. 8 (a) The relative tumor growth curves compared with initial volumes after different treatments (control group, DOX group, IOMSN@uIO(DOX) group, IOMSN@uIO(DOX)-FA group and IOMSN@uIO(DOX)-FA + AMF group). Data are presented as the mean ± standard deviation ($n = 5$). (b) Mean body weights of all treated mice after different treatments. (c) Photographs of mice after 21 days of treatment and (d) relevant H&E histological analysis of tumor tissues. (c) Scale bar = 100 μm. Data are presented as the mean ± standard deviation ($n = 5$). *$p < 0.05$, **$p < 0.005$.

(Fig. 8b) during the treatment. The mice in the DOX group showed rapid tumor growth, indicating that the dosage of administrated free DOX was insufficient to inhibit the tumor growth. Meanwhile, for the mice treated with the IOMSN@uIO(DOX) NPs, the tumor was inhibited in the first 10 days, but recurrence occurred after that, indicating that the passive targeting delivery strategy *via* the ERP effect had a weak delivery efficiency. As is well known, DOX is an effective chemotherapeutic drug for MCF-7 tumors, but it usually requires multiple and high dosages to achieve a satisfying anticancer effect.[34] In comparison, the IOMSN@uIO(DOX)-FA NPs exhibited effective tumor inhibition with no growth of the tumor volume during the 21 days of treatment, which was further confirmed the prominent accumulation of IOMSN@uIO(DOX)-FA NPs at the tumor site induced by active targeting of FA. Because the external AMF could trigger the release rate of DOX from the delivery system, the IOMSN@uIO(DOX)-FA NPs plus AMF led to complete remission of the MCF-7 tumors, as shown in Fig. 8c. The body weight of mice is usually used to evaluate the toxicity of chemotherapeutic agents. As shown in Fig. 8b, no obvious weight loss was observed, implying that the as-synthesized NPs were biocompatible *in vivo*. Haematoxylin and eosin (H&E) staining of the heart, liver, spleen, lung, kidney (Fig. S4†) and tumor (Fig. 8d) in all treatment groups was performed after 21 days. Compared to the control group, no observable changes were found, which further confirmed that the IOMSN@uIO(DOX)-FA NPs with excellent biocompatibility show great potential for use as an MRI-guided stimuli-responsive drug delivery system for effective chemotherapy of cancer.

Conclusions

In summary, highly uniform radial IOMSN@uIO(DOX)-FA NPs exhibiting MRI contrast effects, active targeting properties and stimuli-responsive behaviors were successfully prepared through a simple soft-template process for efficient chemotherapy of cancer. The prepared IOMSN@uIO(DOX)-FA NPs showed high drug loading efficiency and AMF stimuli-responsive release properties, due to the high surface area of their radial mesostructure and induced heating property. Meanwhile, *in vitro* MRI measurements revealed the excellent MRI contrast effect with a high relaxation value of 308 mM^{-1} s^{-1}. Finally, both the *in vitro* and *in vivo* cytotoxicity experiments demonstrated that IOMSN@uIO(DOX)-FA shows great potential as an MRI-guided stimuli-responsive drug delivery system for effective active targeting chemotherapy of cancer.

Experimental section

Materials

Ethylene glycol (EG), diethylene glycol (DEG), sodium acetate anhydrous (NaAc), ammonia solution ($NH_3 \cdot H_2O$), sodium dodecyl benzene sulfonate (SDBS), aminopropyltriethoxysilane (APTES), iron(III) chloride hexahydrate ($FeCl_3 \cdot H_2O$), cetyl trimethyl ammonium bromide (CTAB), diethyl ether ($(C_2H_5)_2O$) and tetraethylorthosilicate (TEOS) were purchased from Aladdin (Shanghai, China). Folic acid (FA), 1-ethyl-3-(3-dimethylaminopropyl)-carbodiimide (EDC), *N*-hydroxysuccinimide (NHS) and dimethylformamide (DMF) were obtained from Sigma-Aldrich (St. Louis, USA). Doxorubicin (DOX) was obtained from Shanghai Jinhe Bio-Technology Co. Ltd (Shanghai, China). RPMI 1640 medium (RPMI 1640), high-glucose Dulbecco's modified Eagle's medium (H-DMEM), fetal bovine serum (FBS), penicillin-streptomycin (PS), and trypsin were purchased from Gibco Life Technologies (Beijing, China). Cell Counting Kit-8 (CCK-8 assay) was provided by Dojindo Molecular Technologies Inc. (Kumamoto, Japan). Coumarin-6, rhodamine phalloidin and DAPI were supplied by Melone Pharmaceutical Co., Ltd. (Dalian, China). Anhydrous ethanol and deionized (DI) water purchased from Sinopharm Chemical Reagent Beijing Co. Ltd. were used throughout. All materials were used without further purification.

Synthesis of larger amino-terminal iron oxide nanoparticles (lIO NPs) and ultra-small iron oxide nanoparticles (uIO NPs)

lIO NPs were synthesized *via* a hydrothermal method, in which Fe^{3+} was partially reduced before the Fe_3O_4 MNPs were formed. Briefly, 1.350 g $FeCl_3 \cdot H_2O$, 2.325 g NaAc and 1.4 g SDBS were added into a mixture of 10 mL EG and 30 mL DEG. Then the mixture was vigorously stirred for 5 h and sealed in a 50 mL Teflon-lined stainless-steel autoclave (with a filling ratio about 70%) at 200 °C for 12 h. After cooling down to room temperature, the product was washed with ethanol and DI water 3 times, then collected by magnetic separation and dried in a vacuum oven at 60 °C for 24 h. Finally, APTES was used as the source of amino groups to modify the lIO NPs under acidic conditions, and lIO NPs were obtained by removing the free APTES. The uIO NPs were synthesized according to a previous method using thermal decomposition.[35]

Preparation of radial Fe_3O_4@SiO_2 mesoporous nanoparticles (IOMSN NPs)

Typically, 1.0 g of CTAB was added into a solution of $NH_3 \cdot H_2O$ (2 mL) and DI water (180 mL). After CTAB had completely dissolved, 35 mL diethyl ether and 50 mL anhydrous ethanol were added. During stirring, 0.2 g lIO NPs, which were homogeneously dispersed in 10 mL anhydrous ethanol, were added into the mixture. After stirring for 10 min, 5 mL of TEOS was added dropwise to the reaction mixture under vigorous stirring at room temperature for another 2 h. The final IOMSN NPs were separated by magnetic separation and washed with DI water and ethanol two times, and eventually dried at 70 °C for 12 h. Finally, the as-prepared IOMSN NPs were calcined in an argon atmosphere at 550 °C for 4 h to remove CTAB.

Preparation of FA-modified IOMSN NPs (IOMSN-FA NPs) and uIO-loaded IOMSN NPs (IOMSN@uIO-FA NPs)

The modification of the surface of IOMSN NPs with FA was achieved through a crosslinker chemistry method. Briefly, 0.2 g of IOMSN NPs were added into 40 mL of anhydrous ethanol containing 0.5 mL of APTES. After being stirred at room temperature for 24 h, the mixture was extensively washed with

ethanol and dried at 80 °C to obtain the IOMSN-NH_2 NPs. Then, 300 mg FA was activated using EDC (86 mg) and NHS (77 mg) dissolved in a DMF/DI water (27 mL, 3 : 1, v/v) solution with stirring for 24 h. Subsequently, the IOMSN-NH_2 NPs (250 mg) were added into the activated FA solution and stirred under anhydrous conditions overnight at room temperature. Finally, the mixture was centrifuged and washed with water and ethanol several times to obtain the IOMSN-FA NPs. To prepare the IOMSN@uIO-FA NPs, uIO NPs were added into an IOMSN-NH_2 NPs solution for another 24 h of stirring before modification with FA.

Drug loading and *in vitro* drug release assay

DOX-loaded IOMSN@uIO(DOX)-FA NPs were synthesized as follows. 1 mL of DOX solution (1 mg mL^{-1} in PBS) was added into 10 mL IOMSN@uIO-FA NPs (100 μg mL^{-1}) in PBS at pH = 7.4. Free DOX was washed away with PBS by centrifugation several times after being stirred overnight. The formed IOMSN@uIO(DOX)-FA NPs were suspended in 1 mL DI water and the loading ratio of DOX was calculated using the UV-vis-NIR spectra of the DOX solution before and after drug loading. To evaluate the DOX release behavior, 1 mL IOMSN@uIO(DOX)-FA NPs were dialyzed against 49 mL PBS in a water bath shaker at 37 °C. At certain time intervals, 1 mL of solution was taken out and tested using the absorbance spectrometer to determine the amount of released DOX and then returned back. The alternative magnetic field (AMF) triggered drug release, and the IOMSN@uIO-FA NPs were exposed to an AMF with a power of 13.33 kA m^{-1} (282 kHz) for 10 min every 24 h.

In vitro cytotoxicity assay and cell uptake

L929 cells obtained from the American Tissue Culture Collection (ATCC) were cultured with H-DMEM supplemented with 10% FBS and 1% penicillin and streptomycin in 5% CO_2 at 37 °C. L929 cells were seeded in a 96-well plate at a density of 5000 cells per well and cultured for 24 h. Then, the old medium was removed and new media containing different concentrations (0, 50, 100, 200 and 500 μg mL^{-1}) of IOMSN@uIO-FA NPs were added, and the cells were incubated for 24 h and 48 h. Cell viability was determined by CCK-8 assay. Before the evaluation of cell uptake efficiency, the green-emitting fluorescent dye, coumarin-6, was attached to the IOMSN@uIO NPs and IOMSN@uIO-FA NPs for the measurement. Typically, MCF-7 cells were seeded in a 24-well plate at a density of 10^4 cells per well and incubated with 50 μg mL^{-1} coumarin-6-loaded IOMSN@uIO NPs and IOMSN@uIO-FA NPs for 1 h, 4 h, and 8 h. The cells were washed with PBS to remove the free nanoparticles and stained with rhodamine phalloidin and DAPI. A confocal laser scanning microscope (CLSM, Zeiss LSM 780, German) was used to view and image the distribution of nanoparticles.

In vitro chemotherapy efficiency

To evaluate the cytotoxicity of the IOMSN@uIO(DOX)-FA NPs, 5000 MCF-7 cells (from the American Tissue Culture Collection (ATCC)) were seeded in 96-well plates for 24 h and then incubated with 200 μL IOMSN@uIO(DOX) NPs and IOMSN@uIO(DOX)-FA NPs suspensions in media at a concentration of 100 μg mL^{-1} for 24 h and 48 h. For the AMF-triggered chemotherapy group, the cells that were incubated with IOMSN@uIO(DOX)-FA NPs were exposed to an AMF with a power of 13.33 kA m^{-1} (282 kHz) for 10 min. At certain time intervals, 100 μL CCK-8 solution was added for another 2 h incubation and then the absorbance was measured with a microplate reader (Varioskan LUX, Thermo Fisher Scientific Inc. Waltham, Massachusetts, USA) at a wavelength of 450 nm. The cytotoxicity was expressed as the percentage of cell viability compared with that of control group.

In vitro MRI measurement

To evaluate the MR imaging property, IOMSN@uIO-FA NPs were suspended in DI water with different Fe concentrations of 0.026, 0.029, 0.032, 0.036 and 0.039 mM. *In vitro* MRI relaxation measurements were conducted on a 3.0 T whole-body MR scanner (Achieva TX, Philips Medical System, Best, The Netherlands) and a turbo spin echo sequence was performed to measure the T_2 relaxation time in terms of Fe with the concentration varying from 0.026 to 0.039 mM.

In vivo anti-tumor efficacy

Balb/c female mice weighing 15–20 g were purchased from Beijing Vital River Laboratory Animal Technology Co., Ltd. and used obeying the protocol no. ZLY16, approved by Tsinghua University Laboratory Animal Research Center (Beijing, China). To determine the anti-tumor efficacy of the IOMSN@uIO(DOX)-FA NPs, the MCF-7 tumor-bearing mice were randomly divided into five groups ($n = 5$): control group i.v. injected with saline (200 μL), DOX group i.v. injected with free DOX (1.5 mg kg^{-1}, 200 μL), IOMSN@uIO(DOX) group i.v. injected with IOMSN@uIO(DOX) NPs (20 mg kg^{-1}, 200 μL), IOMSN@uIO(DOX)-FA group i.v. injected with IOMSN@uIO(DOX)-FA NPs (20 mg kg^{-1}, 200 μL) and IOMSN@uIO(DOX)-FA + AMF group i.v. injected with IOMSN@uIO(DOX)-FA NPs (20 mg kg^{-1}, 200 μL) and exposed to AMF (13.33 kA m^{-1}, 282 kHz) for 10 min every two days. The tumor of each treated mouse was measured with a caliper every other day to calculate the tumor volume using the formula: volume = (tumor length) × (tumor width)^2/2. Relative tumor volume and relative body weight of mice were calculated as V/V_0 (V_0 is the tumor volume when treatment was initiated) and W/W_0 (W_0 is the body weight when treatment was initiated), respectively. After 21 days of treatment, the mice were sacrificed and the main organs (heart, liver, spleen, lung, kidney and tumor) were removed for H&E histological processing and analysis.

Conflicts of interest

There are no conflicts to declare.

Acknowledgements

We are grateful to the National Basic Research Program of China (Grant No. 2013CB932803), the National Key R&D Plan (Grant No. 2016YFC0304502) and the National Natural Science Foundation of China (No. 81671829).

Notes and references

1 B. A. Chabner and T. G. Roberts, *Nat. Rev. Cancer*, 2005, **5**, 65–72.
2 A. Chang, *Lung Cancer*, 2011, **71**, 3–10.
3 W. Xie, Q. Gao, Z. Guo, D. Wang, F. Gao, X. Wang, Y. Wei and L. Zhao, *ACS Appl. Mater. Interfaces*, 2017, **9**, 33660–33673.
4 Q. Wu, Z. Yang, Y. Nie, Y. Shi and D. Fan, *Cancer Lett.*, 2014, **347**, 159–166.
5 Y. Wang, A. Santos, A. Evdokiou and D. Losic, *J. Mater. Chem. B*, 2015, **3**, 7153–7172.
6 B. P. Timko, T. Dvir and D. S. Kohane, *Adv. Mater.*, 2010, **22**, 4925–4943.
7 M. Rezaa Mohammadi, A. Nojoomi, M. Mozafari, A. Dubnika, M. Inayathullah and J. Rajadas, *J. Mater. Chem. B*, 2017, **5**, 3995–4018.
8 R. Jijie, A. Barras, R. Boukherroub and S. Szunerits, *J. Mater. Chem. B*, 2017, **5**, 8653–8675.
9 Y. Zhao, A. C. Tavares and M. A. Gauthier, *J. Mater. Chem. B*, 2016, **4**, 3019–3030.
10 S.-Y. Qin, A.-Q. Zhang, S.-X. Cheng, L. Rong and X.-Z. Zhang, *Biomaterials*, 2017, **112**, 234–247.
11 P. Yingchoncharoen, D. S. Kalinowski and D. R. Richardson, *Pharmacol. Rev.*, 2016, **68**, 701–787.
12 V. P. Torchilin, *Nat. Rev. Drug Discovery*, 2014, **13**, 813–827.
13 W. Xie, Q. Gao, D. Wang, W. Wang, J. Yuan, Z. Guo, H. Yan, X. Wang, X. Sun and L. Zhao, *Int. J. Nanomed.*, 2017, **12**, 7351–7363.
14 A. Martini and C. Ciocca, *Expert Opin. Ther. Pat.*, 2003, **13**, 1801–1807.
15 K. Kataoka, A. Harada and Y. Nagasaki, *Adv. Drug Delivery Rev.*, 2001, **47**, 113–131.
16 C. Barbé, J. Bartlett, L. Kong, K. Finnie, H. Q. Lin, M. Larkin, S. Calleja, A. Bush and G. Calleja, *Adv. Mater.*, 2004, **16**, 1959–1966.
17 B. Delalat, V. C. Sheppard, S. R. Ghaemi, S. Rao, C. A. Prestidge, G. McPhee, M.-L. Rogers, J. F. Donoghue, V. Pillay, T. G. Johns, N. Kröger and N. H. Voelcker, *Nat. Commun.*, 2015, **6**, 8791.
18 Y. Song, Y. Li, Q. Xu and Z. Liu, *Int. J. Nanomed.*, 2016, **12**, 87–110.
19 Y. Wang, Q. Zhao, N. Han, L. Bai, J. Li, J. Liu, E. Che, L. Hu, Q. Zhang, T. Jiang and S. Wang, *Nanomedicine: Nanotechnology, Biology and Medicine*, 2015, **11**, 313–327.
20 J. Lu, M. Liong, J. I. Zink and F. Tamanoi, *Small*, 2007, **3**, 1341–1346.
21 B. Muñoz, A. Rámila, J. Pérez-Pariente, I. Díaz and M. Vallet-Regí, *Chem. Mater.*, 2003, **15**, 500–503.
22 M. Karimi, A. Ghasemi, P. S. Zangabad, R. Rahighi, S. M. M. Basri, H. Mirshekari, M. Amiri, Z. S. Pishabad, A. Aslani, M. Bozorgomid, D. Ghosh, A. Beyzavi, A. Vaseghi, A. R. Aref, L. Haghani, S. Bahrami and M. R. Hamblin, *Chem. Soc. Rev.*, 2016, **45**, 1457–1501.
23 F. Danhier, O. Feron and V. Préat, *J. Controlled Release*, 2010, **148**, 135–146.
24 Y. Zhong, F. Meng, C. Deng and Z. Zhong, *Biomacromolecules*, 2014, **15**, 1955–1969.
25 V. P. Torchilin, *Nat. Rev. Drug Discovery*, 2014, **13**, 813–827.
26 E. G. Kelley, J. N. L. Albert, M. O. Sullivan and I. I. I. T. H. Epps, *Chem. Soc. Rev.*, 2013, **42**, 7057–7071.
27 S. Mura, J. Nicolas and P. Couvreur, *Nat. Mater.*, 2013, **12**, 991–1003.
28 P. Pradhan, J. Giri, F. Rieken, C. Koch, O. Mykhaylyk, M. Döblinger, R. Banerjee, D. Bahadur and C. Plank, *J. Controlled Release*, 2010, **142**, 108–121.
29 C. Sanson, O. Diou, J. Thévenot, E. Ibarboure, A. Soum, A. Brûlet, S. Miraux, E. Thiaudière, S. Tan, A. Brisson, V. Dupuis, O. Sandre and S. Lecommandoux, *ACS Nano*, 2011, **5**, 1122–1140.
30 L. Wang, J. Huang, H. Chen, H. Wu, Y. Xu, Y. Li, H. Yi, Y. A. Wang, L. Yang and H. Mao, *ACS Nano*, 2017, **11**, 4582–4592.
31 F. Tang, L. Li and D. Chen, *Adv. Mater.*, 2012, **24**, 1504–1534.
32 Y. Zhu, T. Ikoma, N. Hanagata and S. Kaskel, *Small*, 2010, **6**, 471–478.
33 A. Espinosa, R. Di Corato, J. Kolosnjaj-Tabi, P. Flaud, T. Pellegrino and C. Wilhelm, *ACS Nano*, 2016, **10**, 2436–2446.
34 M. Zheng, C. Yue, Y. Ma, P. Gong, P. Zhao, C. Zheng, Z. Sheng, P. Zhang, Z. Wang and L. Cai, *ACS Nano*, 2013, **7**, 2056–2067.
35 B. H. Kim, N. Lee, H. Kim, K. An, Y. I. Park, Y. Choi, K. Shin, Y. Lee, S. G. Kwon, H. B. Na, J.-G. Park, T.-Y. Ahn, Y.-W. Kim, W. K. Moon, S. H. Choi and T. Hyeon, *J. Am. Chem. Soc.*, 2011, **133**, 12624–12631.

